Multi-wavelength quantitative polarization and phase microscope

Xiaobo Tian,[1] Xingzhou Tu,[1] Kimiko Della Croce,[2] Guang Yao,[2,3] Haijiang Cai,[4] Neal Brock,[5] Stanley Pau,[1] and Rongguang Liang[1,*]

[1]*College of Optical Science, University of Arizona, Tucson, AZ 85721, USA*
[2]*Department of Molecular & Cellular Biology, University of Arizona, Tucson, AZ 85721, USA*
[3]*Arizona Cancer Center, University of Arizona, Tucson, AZ 85721, USA*
[4]*Department of Neuroscience, University of Arizona, Tucson, AZ 85721, USA*
[5]*4D Technology Corporation, Tucson, Arizona 85706, USA*
*rliang@optics.arizona.edu

Abstract: We introduce a snapshot multi-wavelength quantitative polarization and phase microscope (MQPPM) for measuring spectral dependent quantitative polarization and phase information. The system uniquely integrates a polarized light microscope and a snap-shot quantitative phase microscope in a single system, utilizing a novel full-Stokes camera operating in the red, green, and blue (RGB) spectrum. The linear retardance and fast axis orientation of a birefringent sample can be measured simultaneously in the visible spectra. Both theoretical analysis and experiments have been performed to demonstrate the capability of the proposed microscope. Data from liquid crystal and different biological samples are presented. We believe that MQPPM will be a useful tool in measuring quantitative polarization and phase information of live cells.

1. Introduction

Measurement of quantitative phase and optical anisotropy information has long been of interest for biomedical researchers. Various microscopic techniques have been developed to obtain quantitative phase information from biological samples, including Fourier phase microscopy [1], digital holographic microscopy [2], Hilbert phase microscopy [3], diffraction phase microscopy [4], tomographic phase microscopy [5] and polarization phase microscopy [6]. Similarly, quantitative polarized light microscopy [7–10] has been developed to acquire the birefringence information. Recently methods that combine quantitative phase and birefringence measurement in a single system have been proposed in [11,12]. In all these methods, the phase or birefringence information was measured with a single wavelength.

Multi-wavelength techniques contribute to the measurement in many aspects [13]. The 2π ambiguities in unwrapping can be removed using multi-wavelength techniques [14,15]. Dual-wavelength and multi-wavelength techniques can also be used to solve the focusing problem [16] and the chromatic aberration [17]. Cells with different protein concentration can be distinguished by measuring the refractive index of cells [18,19]. Since the phase depends on both thickness and refractive index, more than one wavelength is usually required to separate the thickness and refractive index of the sample [20]. The wavelength-dependent refractive index can be determined with spectroscopic phase microscopy [21], spectroscopic diffraction phase microscopy [22], quantitative dispersion microscopy [23], quantitative phase spectroscopy [24], dynamic spectroscopic phase microscopy [25] and white light interference microscopy [26].

We propose a snapshot multi-wavelength quantitative polarization and phase microscope (MQPPM) using a customized CMOS camera with linear micro-polarizer and Bayer filters [27]. It can obtain single-shot measurement of quantitative birefringence and phase information in RGB spectra.

2. Quantitative polarization and phase microscope system

2.1 System layout

Our MQPPM is based on a Linnik interferometer as shown in Fig. 1. Three light emitting diodes (LEDs) in red (M625L4), green (M530L3) and blue (M455L3) from Thorlabs Inc. provide the multi-wavelength illumination. The central wavelength of each bandpass filters are 460 nm, 540 nm and 630 nm with a bandwidth of 10 nm for green, blue and red LEDs respectively. The light emitted from the LEDs is collimated by an achromatic lens (L1) and passes through a polarizer (P) with transmission axis at 0° relative to the optical axis, then is split into two light beams by a non-polarizing beam splitter (BS). Two identical microscope objectives (MO1 and MO2) are used to match the optical path lengths for the multiple wavelength spectrum. In the sample arm, light passes through an achromatic quarter waveplate (QWP1) with fast axis at 45° relative to optical axis, which transforms linear polarized light to circular polarized light. This circular polarized light after passing through the sample is reflected by a flat mirror. In the reference arm, an achromatic quarter waveplate (QWP2) with fast axis of 0° is inserted between the BS and the reference mirror. The polarization is maintained after passing through QWP2. This QWP2 is used for matching the optical path length and can be replaced by an optical window with the same optical thickness of the QWP1. A customized RGB full Stokes camera was built to capture the polarization images of the sample at three wavelengths simultaneously. This camera consists of a non-polarizing beam splitter, one achromatic quarter waveplate (QWP3), one glass compensation plate with the same thickness as the achromatic QWP3, and two customized color polarization cameras (4D Technology, PolarCam[TM] [28]) with a wire-grid micro-polarizer array on the standard RGB Bayer filter array [16]. For the birefringence measurement, the reference arm is blocked and this system works as a polarized light microscope.
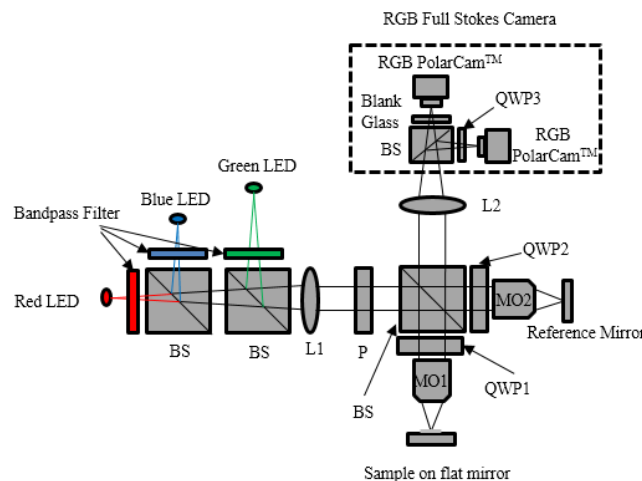

Fig. 1. System layout of the snapshot multi-wavelength quantitative polarization and phase microscope (MQPPM). BS: non-polarizing beams splitter; L1 and L2: lens; P: polarizer; QWP1, QWP2 and QWP3: achromatic quarter waveplate; MO1 and MO2: microscope objective; RGB PolarCam: custom camera constructed by 4D Technology with a wire-grid micro-polarizer array on the standard RGB Bayer filter array.

2.2 Operating principle

Polarization is often described in terms of the four parameters of the Stokes vector S. With electric field vectors E_x in x direction and E_y in y direction, the Stokes vector is given by

$$S = \begin{bmatrix} S_0 \\ S_1 \\ S_2 \\ S_3 \end{bmatrix} = \begin{bmatrix} E_x E_x^* + E_y E_y^* \\ E_x E_x^* - E_y E_y^* \\ E_x E_y^* + E_y E_x^* \\ i(E_x E_y^* - E_y E_x^*) \end{bmatrix} \tag{1}$$

where S_0 is the absolute intensity, S_1 describes the amount of light polarized along the horizontal or the vertical axes, S_2 describes the amount of light polarized along 45° or 135°, and S_3 describes the amount of right or left circularly polarized light. The full Stokes vector parameters are acquired using the algorithms described in reference [27] Appendix C.

For a sample with only birefringence information, the polarization property can be described by Jones calculus. The Jones vectors of the test arm is

$$E_T = QWP(-45) * S(\phi,\delta,-\alpha) * M_R * S(\phi,\delta,\alpha) * QWP(45) * E_{in} \tag{2}$$

where $E_{in} = \begin{bmatrix} 1 \\ 0 \end{bmatrix}$ is the incident Jones vector of the beam after passing through the linear

polarizer at 0°, $QWP(\alpha) = R(-\alpha) \begin{bmatrix} e^{i\pi/4} & 0 \\ 0 & e^{-i\pi/4} \end{bmatrix} R(\alpha)$ is the Jones matrix of the quarter wave

plate with fast axis aligned at angle α, and $R(\alpha) = \begin{bmatrix} \cos\alpha & \sin\alpha \\ -\sin\alpha & \cos\alpha \end{bmatrix}$ is a rotation matrix.

$M_R = \begin{bmatrix} 1 & 0 \\ 0 & -1 \end{bmatrix}$ is the Jones matrix of the dielectric mirror. The Jones matrix of a

birefringence sample is written as:

$$S(\phi,\delta,\alpha) = e^{-i\phi} R(-\alpha) \begin{bmatrix} e^{i\delta/2} & 0 \\ 0 & e^{-i\delta/2} \end{bmatrix} R(\alpha) \tag{3}$$

where δ is the retardation, α is the angle of fast axis and ϕ is the phase.

After inserting the Jones matrices into Eq. (2), the Jones vector of the beam returning from the test arm becomes

$$E_T = \begin{bmatrix} e^{-2i(\phi+\alpha)} \sin\delta \\ e^{-2i\phi} \cos\delta \end{bmatrix}, \tag{4}$$

and the Jones vector of the beam in the reference arm is

$$E_R = QWP(0) * M_R * QWP(0) * E_{in} = \begin{bmatrix} 1 \\ 0 \end{bmatrix} \tag{5}$$

2.2.1 Birefringence measurement

To measure the birefringence of a sample, the reference arm is blocked. This system works as a quantitative polarized light microscope. The retardance and fast axis of the birefringence sample can be measured simultaneously. After inserting Eq. (4) into Eq. (1), the output Stokes vector of the birefringence sample is

$$S_T = \begin{bmatrix} S_{T0} \\ S_{T1} \\ S_{T2} \\ S_{T3} \end{bmatrix} = \begin{bmatrix} 1 \\ -\cos 2\delta \\ \cos 2\alpha \sin 2\delta \\ \sin 2\alpha \sin 2\delta \end{bmatrix}. \tag{6}$$

Then the fast axis angle and retardance can be calculated by

$$\alpha = \frac{1}{2} \arctan(\frac{S_{T3}}{S_{T2}}), \tag{7}$$

$$\delta = \frac{1}{2} \arctan \frac{\sqrt{S_{T2}^2 + S_{T3}^2}}{-S_{T1}}. \tag{8}$$

The calculated retardance has an ambiguity when the retardance is between $\pi/2$ to π. This ambiguity could be unwrapped to get absolute retardance in a depth resolved imaging system [29]. However, without prior knowledge of the birefringence of the sample, the range of retardance is undetermined. In addition, S_{T2} and S_{T3} are close to 0 when the retardance is close to $n\pi/2$, which could lead to discontinuity for the fast axis calculation. This discontinuity problem can be improved by combining the results from the different RGB wavelengths.

2.2.2 Phase measurement

In quantitative phase microscope mode with both test and reference arms on, the Jones vector of the optical field represented by the interferogram is

$$E = E_T + E_R = \begin{bmatrix} e^{-2i(\phi+\alpha)} \sin \delta + 1 \\ e^{-2i\phi} \cos \delta \end{bmatrix} \tag{9}$$

and the Stokes vector is:

$$S = \begin{bmatrix} 1 \\ -\cos 2\delta \\ \cos 2\alpha \sin 2\delta \\ \sin 2\alpha \sin 2\delta \end{bmatrix} + \begin{bmatrix} 1 \\ 1 \\ 0 \\ 0 \end{bmatrix} + 2 \begin{bmatrix} \cos(2\alpha+2\phi)\sin \delta \\ \cos(2\alpha+2\phi)\sin \delta \\ \cos \delta \cos 2\phi \\ -\cos \delta \sin 2\phi \end{bmatrix} = S_T + S_R + 2S_F \tag{10}$$

where $S_R = \begin{bmatrix} 1 \\ 1 \\ 0 \\ 0 \end{bmatrix}$ is the Stokes vector for the reference arm and

$S_F = \begin{bmatrix} S_{F0} \\ S_{F1} \\ S_{F2} \\ S_{F3} \end{bmatrix} = \begin{bmatrix} \cos(2\alpha+2\phi)\sin \delta \\ \cos(2\alpha+2\phi)\sin \delta \\ \cos \delta \cos 2\phi \\ -\cos \delta \sin 2\phi \end{bmatrix}$ is the Stokes vector for the interference term between the

sample and reference arms. S_F can be separated from S by Fourier transform or subtracting the Stokes vector of the sample and reference arms. The birefringence-induced phase error is corrected using the birefringence data. The phase can be calculated by

$$\phi = \frac{1}{2} \arctan \left(-\frac{S_{F3}}{S_{F2}} \right). \tag{11}$$

If the sample has no birefringence, i.e. when retardance $\delta = 0$, then Eq. (10) can be simplified as

$$S = \begin{bmatrix} 2 \\ 0 \\ 2\cos 2\phi \\ -2\sin 2\phi \end{bmatrix}.$$
(12)

The phase can be calculated from a single-shot measurement by

$$\phi = \frac{1}{2}\arctan\left(-\frac{S_3}{S_2}\right).$$
(13)

3. Experimental results

The spectrum of the light source is an important factor in phase and birefringence measurement. In order to obtain more accurate measurement, a bandpass filter with 10nm bandwidth is used in front of each LED. The spectrum of RGB light source is measured by a spectrometer and shown in Fig. 2.
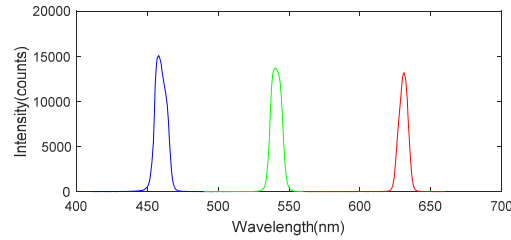

Fig. 2. Spectrum for RGB LED light source.

To verify the accuracy of the system, a waveplate was measured with the fast axis rotating from 0° to 180° in steps of 10° under a 10X NA 0.28 objective. The retardance was measured by an AxoScan Mueller matrix polarimeter, as shown in Fig. 3. The measured retardances at 460 nm (B), 540 nm (G), and 630 nm (R) are 131°, 104°, and 85° respectively. For a sample with retardance larger than $\pi/2$, the absolute retardance should be calculated by Eq. (14) due to the ambiguity in the measured retardance. In order to get absolute retardance, the range of retardance must be determined first.

$$\delta = \begin{cases} n\pi + \dfrac{1}{2}\arctan\dfrac{\sqrt{S_{T2}^2 + S_{T3}^2}}{-S_{T1}}, & n\pi \leq \delta < (n+\dfrac{1}{2})\pi \\ (n+1)\pi - \dfrac{1}{2}\arctan\dfrac{\sqrt{S_{T2}^2 + S_{T3}^2}}{-S_{1T}}, & (n+\dfrac{1}{2})\pi \leq \delta < (n+1)\pi \end{cases}.$$
(14)

Based on the knowledge that the retardance for the R channel is in the range $(0, \pi/2)$, while that for the G and the B are in the range $(\pi/2, \pi)$, the retardance ambiguity can be removed. The measured retardance after removing ambiguity for R, G and B is shown in Fig. 4(a). The measured retardance at the R channel is 84.44° with a standard deviation of 1.01°, at the G channel is 103.02° with a standard deviation of 2.12°, and at the B channel is 129.63° with a standard deviation of 3.05°, showing good agreement with the measured value in Fig. 3. The measured fast axis orientation is shown in Fig. 4(b). The standard deviations of the difference between the measured and actual data are 2.75°, 3.79° and 3.01° at the R, G and B

channels. The errors in retardance and fast axis orientation are caused by imperfect optical components and the limitation of the manually controlled rotational mounts.
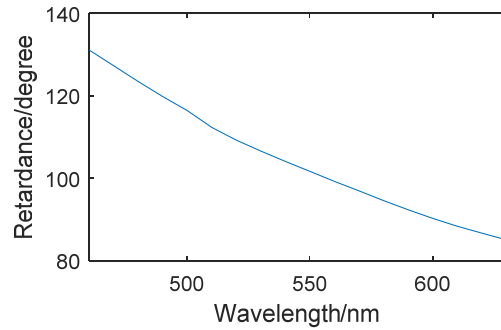

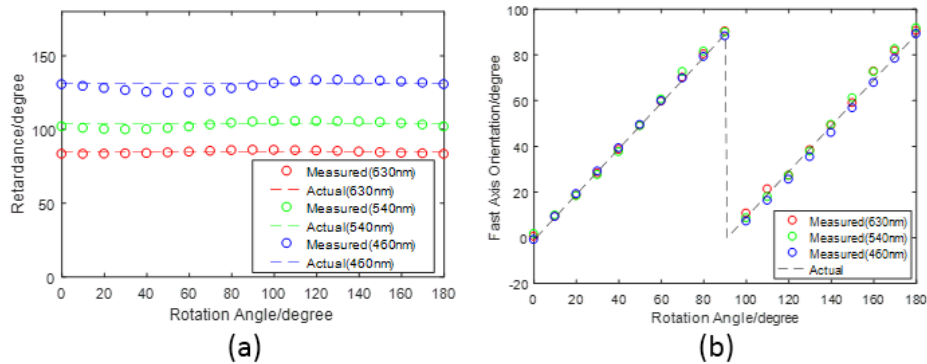Fig. 3. The retardance of waveplate measured by AxoScan Mueller matrix polarimeter.

Fig. 4. (a) Retardance and (b) fast axis orientation angle of the waveplate at RGB spectrum as a function of rotation angle from 0° to 180° with 10° steps.

The phase measurement was calibrated using a step height standard (VLSI, SHS 4606 Å) using the 10X NA 0.28 and the 30X NA 0.65 objectives. The step height standard is measured 10 times, calculated and averaged in accordance to the definition in ISO 5436-1 standard. Figure 5 shows the 3D surface and line profile of the step height standard measured by our system in the R channel with 30X NA 0.65 objective. The averaged measured step height is 460.37 nm with a standard deviation of 1.87 nm, as shown in Table 1.
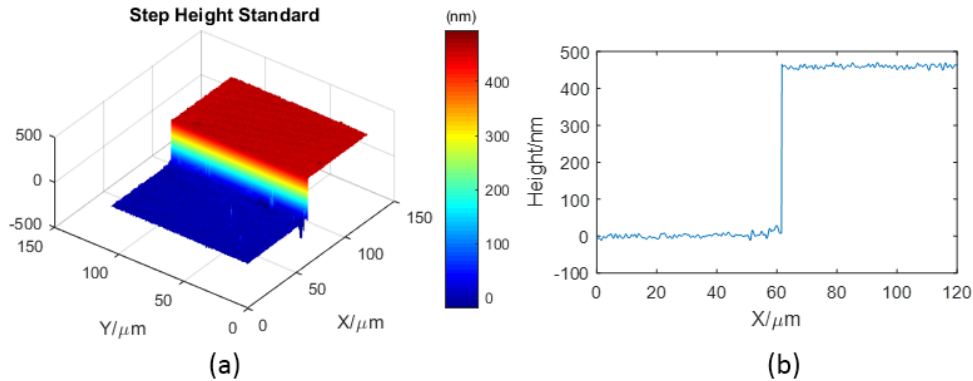
Fig. 5. System calibration using a step height measurement. (a) 3D surface and (b) line profile of a step height standard.

Table 1. Measurement results of the VLSI step height standard from the R channel.

No.	Step Height (nm)	No.	Step Height (nm)
1	459.76	6	461.26
2	456.85	7	458.98
3	462.09	8	460.30
4	460.82	9	463.89
5	460.04	10	459.78
Mean value	460.37		
Std. Dev.	1.87		

3.1 Birefringent sample

To demonstrate the capability of birefringence measurement, a drop of liquid crystal was used as a birefringent sample. The retardance calculated by Eq. (8) for the R, G and B channels are shown in Figs. 6(a)-6(c). Based on Eq. (14) we know that there is an ambiguity problem where the retardance is larger than $\pi/2$. With a prior knowledge that the left side of the figure was a flat mirror with zero retardance and the thickness of the liquid crystal drop increased from left to right, the range of the retardance can be determined by calculating the retardance slope. The retardance was firstly smoothed with a low pass filter to get rid of the influence of surface roughness, then the retardance slope for each point (x, y) was calculated by $\delta(x+1, y) - \delta(x, y)$. Any point (x, y) with a minus slope was considered in the range of $(n+\frac{1}{2})\pi \leq \delta < (n+1)\pi$, a minus sign was given to the retardance. The wrapped retardances were then generated and shown in Figs. 6(d)-6(f). The unwrapped retardance are shown in Figs. 6(g)-6(i).

The fast axis orientation of the R, G and B channels are shown in Figs. 7(a)-7(c). Two kinds of discontinuities are observed in the fast axis orientation map. The first discontinuity is due to the modulo nature of the arctangent function. The second discontinuity is caused by the fact that both the denominator and the numerator are zero in Eq. (7) when the retardance is equal to $n\pi/2$. The second discontinuity is retardance-related and wavelength-dependent, it can be reduced by combining the fast axis orientation in three wavelengths. To combine the three different wavelengths, the fast axis of the R channel is used first since the standard deviation for R channel is the smallest. If the retardance of one pixel in the R channel is less than 5° or greater than 85°, then the fast axis orientation of the R channel is considered unreliable and the fast axis of this pixel is replaced with that of the G channel. If the

retardance of the G channel is still less than 5° or greater than 85°, then the fast axis of this pixel is replaced with that of the B channel. In the case that the retardances of the RGB channels are less than 5° or greater than 85°, the fast axis orientation is defined to be zero. The fast axis orientation map after combining three wavelength is shown in Fig. 7(d).
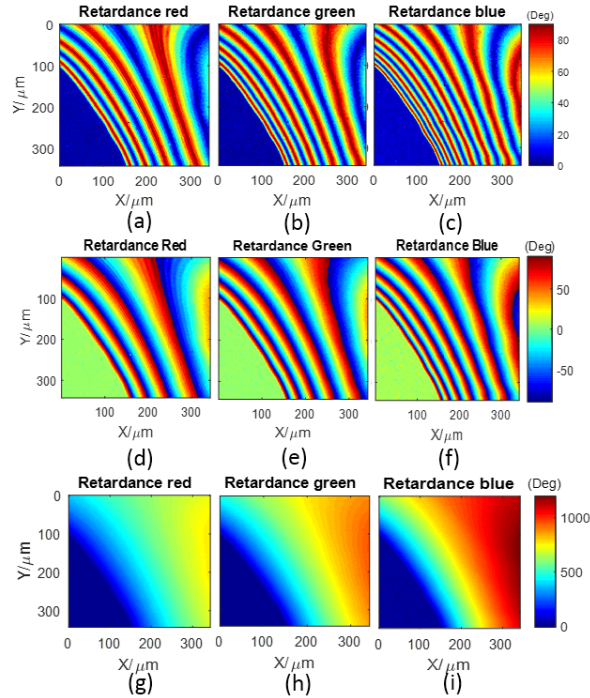

Fig. 6. Measured retardance of liquid crystal in (a) red, (b) green and (c) blue. Wrapped retardance of liquid crystal in (d) red, (e) green and (f) blue. Unwrapped retardance of liquid crystal in (g) red, (h) green and (i) blue.
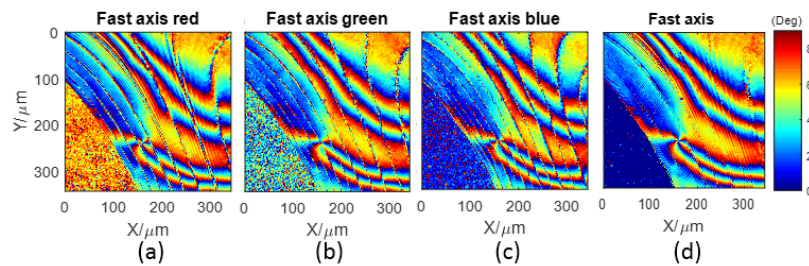

Fig. 7. Fast axis orientation in (a) red, (b) green, (c) blue and (d) combined result of RGB.

In order to obtain the phase information, two separate measurements are needed. The Stokes images are taken in both quantitative phase microscope mode and polarized light microscope mode. With a priori recorded reference measurement, the interferogram term is separated by subtracting the birefringence and reference terms. Then the phase is calculated using Eq. (11). The wrapped phase of the liquid crystal in the R, G and B channels are shown in Figs. 8(a)-8(c). Similar to the fast axis orientation, two kinds of discontinuities are observed in the phase map. One is caused by the modulo nature of arctangent function, and the second is due to the fact that both denominator and numerator are zero in Eq. (11) when the retardance equals to $(n+\frac{1}{2})\pi$. Due to the chromatic aberration and the limitation of the

coherence length, the contrast of the interferograms in the blue channel drops faster than red and green, causing the increased noise in the blue channel as the thickness of liquid crystal increased.
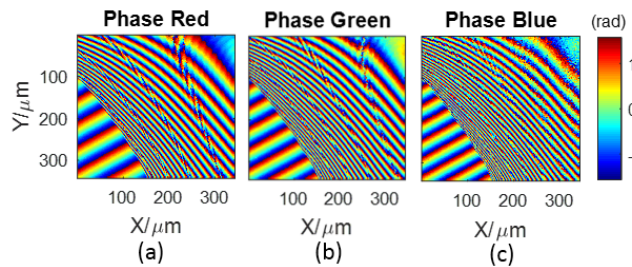

Fig. 8. Wrapped phase of liquid crystal in (a) red, (b) green and (c) blue channels.

3.2 Biological samples

To demonstrate MQPPM's performance in real time imaging of biological samples, the red blood cells (RBCs) and human breast cancer cells were measured with the prototype system. Transparent biological cells were placed on a mirror in their growth media. Since the measured retardance of RBCs and human breast cancer cells are much smaller than the phase of these cells, these cells are considered as non-birefringent samples. The measured phase is the optical path length, the product of the refractive index and physical thickness.

Figure 9(a) shows the phase map of several RBCs in the red channel. Figures 9(b)-5(d) show the three dimensional (3-D) images of one RBC in the R, G and B channels, and Fig. 9(e) shows the corresponding profiles of this cell. The figure shows that the OPD is larger for shorter wavelength due to the larger refractive index at shorter wavelength. The measurement was performed using a 30X NA 0.65 objective.

Figure 10 shows the dynamic measurement of human breast cancer cells after the growth media was diluted by purified water. Purified water was added at zero minute and 8 minutes in Fig. 10(a) and Fig. 10(c). The cells osmotically swell after exposure to purified water in Fig. 10(a)-10(b). In Fig. 10(c)-10(d), swelling and flattening were observed after the cells were exposed to more purified water. The measurement was performed using a 10X NA 0.28 objective.
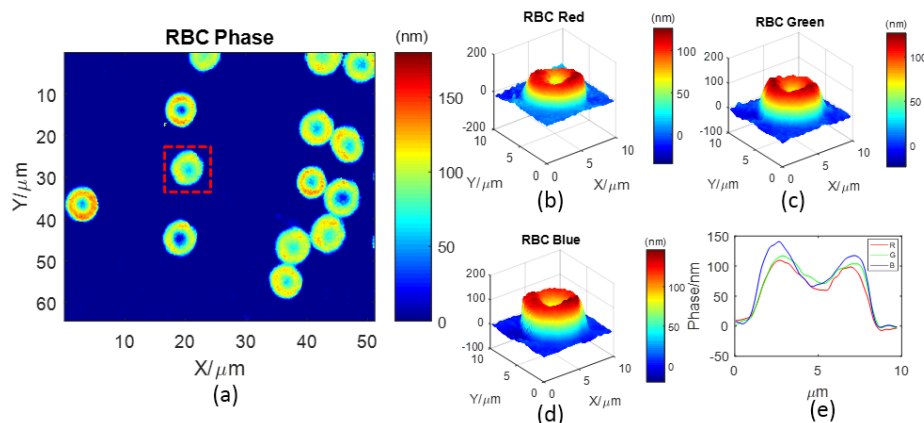

Fig. 9. Measurement results of red blood cells (RBCs). (a) RBC phase in R channel, (b)-(d) 3-D images of one cell in the R, G and B channels, and (e) the phase profile of one cell in different wavelengths.
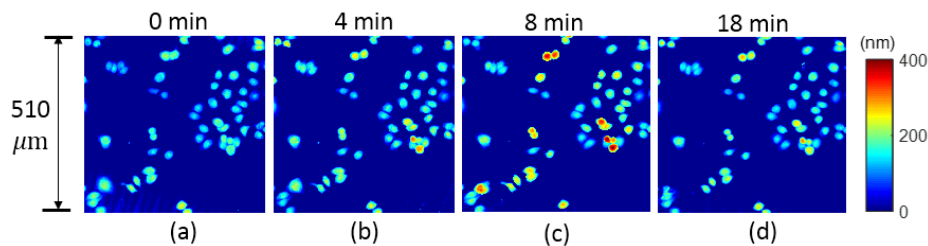
Fig. 10. Time series of phase images of breast cancer cells after contact with purified water. (a)-(b) Cells osmotically swell after exposure to purified water. (c)-(d) Cells swell and flatten after more purified water were added. Movies were taken with sampling times of a few seconds over 18 minutes (Visualization 1).

4. Conclusion

In summary, we have developed, calibrated, and demonstrated a snapshot multi-wavelength quantitative polarization and phase microscope (MQPPM) for measurement of both the birefringence and phase information in the RGB spectrums. This microscope can measure wavelength-dependent retardance, fast axis orientation and quantitative phase of the biological samples in real time.

Funding

Disclosures

The authors declare that there are no conflicts of interest related to this article.

References

1. G. Popescu, L. P. Deflores, J. C. Vaughan, K. Badizadegan, H. Iwai, R. R. Dasari, and M. S. Feld, "Fourier phase microscopy for investigation of biological structures and dynamics," Opt. Lett. **29**(21), 2503–2505 (2004).
2. B. Rappaz, P. Marquet, E. Cuche, Y. Emery, C. Depeursinge, and P. Magistretti, "Measurement of the integral refractive index and dynamic cell morphometry of living cells with digital holographic microscopy," Opt. Express **13**(23), 9361–9373 (2005).
3. T. Ikeda, G. Popescu, R. R. Dasari, and M. S. Feld, "Hilbert phase microscopy for investigating fast dynamics in transparent systems," Opt. Lett. **30**(10), 1165–1167 (2005).
4. G. Popescu, T. Ikeda, R. R. Dasari, and M. S. Feld, "Diffraction phase microscopy for quantifying cell structure and dynamics," Opt. Lett. **31**(6), 775–777 (2006).
5. W. Choi, C. Fang-Yen, K. Badizadegan, S. Oh, N. Lue, R. R. Dasari, and M. S. Feld, "Tomographic phase microscopy," Nat. Methods **4**(9), 717–719 (2007).
6. K. Creath and G. Goldstein, "Dynamic quantitative phase imaging for biological objects using a pixelated phase mask," Biomed. Opt. Express **3**(11), 2866–2880 (2012).
7. I. H. Shin, S. M. Shin, and D. Y. Kim, "New, simple theory-based, accurate polarization microscope for birefringence imaging of biological cells," J. Biomed. Opt. **15**(1), 016028 (2010).
8. M. Shribak, "Complete polarization state generator with one variable retarder and its application for fast and sensitive measuring of two-dimensional birefringence distribution," J. Opt. Soc. Am. A **28**(3), 410–419 (2011).
9. S. Sugita and T. Matsumoto, "Quantitative measurement of the distribution and alignment of collagen fibers in unfixed aortic tissues," J. Biomech. **46**(7), 1403–1407 (2013).
10. C. Li and Y. Zhu, "Quantitative polarized light microscopy using spectral multiplexing interferometry," Opt. Lett. **40**(11), 2622–2625 (2015).
11. S. Aknoun, P. Bon, J. Savatier, B. Wattellier, and S. Monneret, "Quantitative retardance imaging of biological samples using quadriwave lateral shearing interferometry," Opt. Express **23**(12), 16383–16406 (2015).
12. C. Li, S. Chen, M. Klemba, and Y. Zhu, "Integrated quantitative phase and birefringence microscopy for imaging malaria-infected red blood cells," J. Biomed. Opt. **21**(9), 090501 (2016).
13. B. Yayebi, J. h. Kim, and J. H. Han, "Review on multi-wavelength quantitative phase microscopy," in 2016 4th international Winter Conference on Brain-Computer Interface, 1–2 (2016).
14. C. J. Mann, P. R. Bingham, V. C. Paquit, and K. W. Tobin, "Quantitative phase imaging by three-wavelength digital holography," Opt. Express **16**(13), 9753–9764 (2008).

15. N. Warnasooriya and M. K. Kim, "LED-based multi-wavelength phase imaging interference microscopy," Opt. Express **15**(15), 9239–9247 (2007).
16. M. R. Jafarfard, S. Moon, B. Tayebi, and D. Y. Kim, "Dual-wavelength diffraction phase microscopy for simultaneous measurement of refractive index and thickness," Opt. Lett. **39**(10), 2908–2911 (2014).
17. P. Gao, B. Yao, R. Rupp, J. Min, R. Guo, B. Ma, J. Zheng, M. Lei, S. Yan, D. Dan, and T. Ye, "Autofocusing based on wavelength dependence of diffraction in two-wavelength digital holographic microscopy," Opt. Lett. **37**(7), 1172–1174 (2012).
18. P. Ferraro, S. Grilli, L. Miccio, D. Alfieri, S. De Nicola, A. Finizio, and B. Javidi, "Full color 3-D imaging by digital holography and removal of chromatic aberrations," J. Disp. Technol. **4**(1), 97–100 (2008).
19. A. Wax, C. Yang, V. Backman, K. Badizadegan, C. W. Boone, R. R. Dasari, and M. S. Feld, "Cellular organization and substructure measured using angle-resolved low-coherence interferometry," Biophys. J. **82**(4), 2256–2264 (2002).
20. Y. Park, M. Diez-Silva, G. Popescu, G. Lykotrafitis, W. Choi, M. S. Feld, and S. Suresh, "Refractive index maps and membrane dynamics of human red blood cells parasitized by Plasmodium falciparum," Proc. Natl. Acad. Sci. U.S.A. **105**(37), 13730–13735 (2008).
21. Y. Park, T. Yamauchi, W. Choi, R. Dasari, and M. S. Feld, "Spectroscopic phase microscopy for quantifying hemoglobin concentrations in intact red blood cells," Opt. Lett. **34**(23), 3668–3670 (2009).
22. H. Pham, B. Bhaduri, H. Ding, and G. Popescu, "Spectroscopic diffraction phase microscopy," Opt. Lett. **37**(16), 3438–3440 (2012).
23. D. Fu, W. Choi, Y. Sung, Z. Yaqoob, R. R. Dasari, and M. Feld, "Quantitative dispersion microscopy," Biomed. Opt. Express **1**(2), 347–353 (2010).
24. M. Rinehart, Y. Zhu, and A. Wax, "Quantitative phase spectroscopy," Biomed. Opt. Express **3**(5), 958–965 (2012).
25. Y. Jang, J. Jang, and Y. Park, "Dynamic spectroscopic phase microscopy for quantifying hemoglobin concentration and dynamic membrane fluctuation in red blood cells," Opt. Express **20**(9), 9673–9681 (2012).
26. D. S. Mehta and V. Srivastava, "Quantitative phase imaging of human red blood cells using phase-shifting white light interference microscopy with colour fringe analysis," Appl. Phys. Lett. **101**(20), 203701 (2012).
27. X. Tu, O. J. Spires, X. Tian, N. Brock, R. Liang, and S. Pau, "Division of amplitude RGB full-Stokes camera using micro-polarizer arrays," Opt. Express **25**(26), 33160–33175 (2017).
28. N. J. Brock, J. E. Millerd, J. C. Wyant, and J. B. Hayes, "Pixelated phase-mask interferometer," U.S. Patent, 7,230,717 (12 June 2007).
29. C. Fan and G. Yao, "Mapping local retardance in birefringent samples using polarization sensitive optical coherence tomography," Opt. Lett. **37**(9), 1415–1417 (2012).